ACS OMEGA

http://pubs.acs.org/journal/acsodf

Article

Hydrogenation of Toluene to Methyl Cyclohexane over PtRh Bimetallic Nanoparticle-Encaged Hollow Mesoporous Silica Catalytic Nanoreactors

Kaijie Li,[†] Heliang An,[†] Peijian Yan, Caoping Yang, Tao Xiao, Junyou Wang, and Shenghu Zhou*

Cite This: *ACS Omega* 2021, 6, 5846−5855

Read Online

ACCESS | Metrics & More | Article Recommendations | Supporting Information

ABSTRACT: PtRh bimetallic nanoparticle (NP)-encaged hollow mesoporous silica nanoreactors (PtRh@HMSNs) are prepared by employing metal-ion-containing charge-driven polymer micelles as templates. These nanoreactors feature ∼1−2 nm PtRh NPs in ∼11 nm hollow cavities of HMSNs. Among various Pt_xRh_y@HMSNs, $Pt_{0.77}Rh_1$@HMSNs show the best catalytic performance for toluene hydrogenation. Under 30 °C, atmospheric H_2 pressure, and a toluene/(Pt+Rh) molar ratio of 200/1, $Pt_{0.77}Rh_1$@HMSNs reach 100.0% of methyl cyclohexane yield and demonstrate a much better catalytic performance than monometallic Pt@HMSNs and Rh@HMSNs and their physical mixtures. Moreover, $Pt_{0.77}Rh_1$@HMSNs exhibit a good catalytic stability during recycling experiments. The enhanced performance of $Pt_{0.77}Rh_1$@HMSNs is ascribed to the interaction between Pt and Rh, the beneficial effect of the relatively large mesoporous channels for mass transfer, as well as the confinement effect of functional NPs inside hollow cavities.

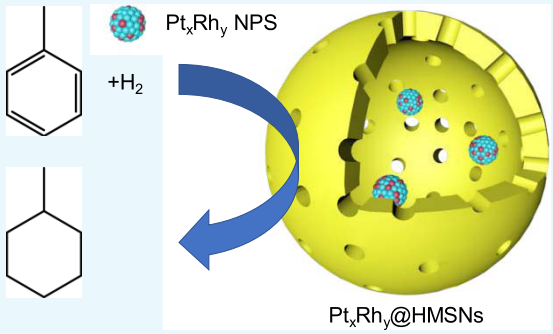

1. INTRODUCTION

Hydrogen is well recognized as a clean and environmentally friendly energy source.[1] However, due to its characteristics of large diffusion coefficient, wide explosion limit, and low ignition temperature, H_2 energy has not been used on a large scale.[2] To safely use H_2 energy, storage and transport of hydrogen securely and expeditiously are prerequisites. Instead of H_2 gas, liquid organic hydrogen carriers,[3,4] adsorbing materials,[5−7] and metal hydrides[8−10] can safely store and release H_2 and are considered as alternative H_2 energy sources. Among these mentioned chemicals, liquid organic hydrogen carriers are composed of unsaturated aromatics and their corresponding liquid organic hydrogen carriers, such as benzene/cyclohexane[11,12] and toluene/methyl cyclohexane,[13−15] which can be hydrogenated and dehydrogenated reversibly without destroying the main structure of the carbon ring. Due to their easy transportation and low toxicity, toluene/methyl cyclohexane is a good candidate for H_2 storage and utilization.

Transition metals including Ni,[16] Pt,[17] Ru,[18,19] and Rh[13,14,17,20,21] have been studied in hydrogenation of toluene to methyl cyclohexane. To achieve high yields of methyl cyclohexane, non-noble metals such as Ni catalysts usually require relatively high reaction temperatures, while noble metals such as Rh can perform hydrogenation under room temperature and atmospheric H_2 pressure. In addition, PtRh bimetallic catalysts are selected for toluene hydrogenation because they could have a better performance due to the synergistic effect. For instance, Miyamura and co-workers reported a polysilane-immobilized PtRh catalyst for hydrogenation of toluene to methyl cyclohexane with a high yield (>99%) under the reaction conditions of 50 °C, 0.1 MPa of H_2, and 20 h.[22] Al_2O_3-supported PtRh catalysts achieve a yield of 90% at 22 °C, 0.1 MPa H_2, and 7 h.[17] The underlying principle is to utilize the metal−metal interaction to adjust the electronic state of the active metals,[23,24] resulting in the enhanced catalytic performance of bimetallic systems.

In the last decades, hollow nanoreactors[25−27] have been considered as good supports due to the confinement effect related to their small size and encapsulation of metal nanoparticles (NPs) into mesoporous silica, which have attracted more attention. Due to the protection effect of mesoporous silica shells, the synthesized materials such as Pt@$mSiO_2$ show a significantly enhanced catalytic stability for high temperature reactions.[28] Moreover, mesoporous silica shells can facilitate the mass transportation for reactions relative to the microporous materials. Recently, our group reported the synthesis of hollow mesoporous nanoreactors with encaged functional NPs using charge-driven micelles as templates. By

Received: December 24, 2020
Accepted: February 3, 2021
Published: February 15, 2021

https://dx.doi.org/10.1021/acsomega.0c06268
ACS Omega 2021, 6, 5846−5855

Scheme 1. Schematic Demonstration of the Synthetic Route for Pt_xRh_y@HMSNs

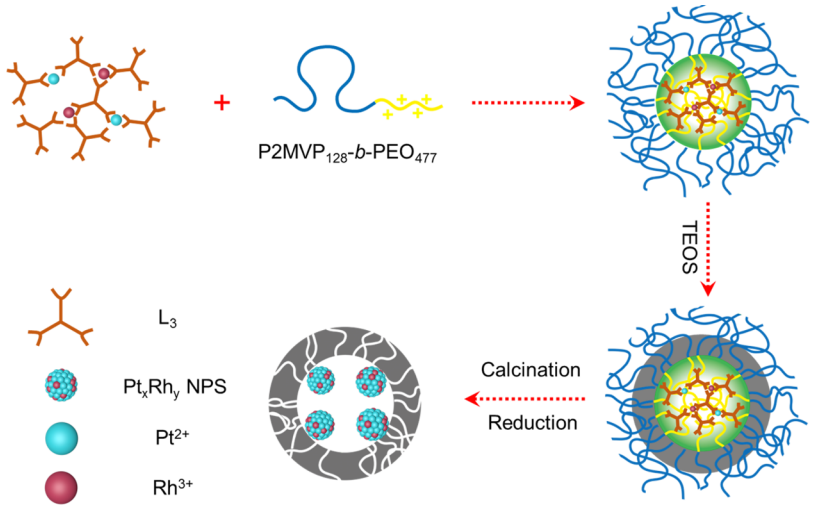

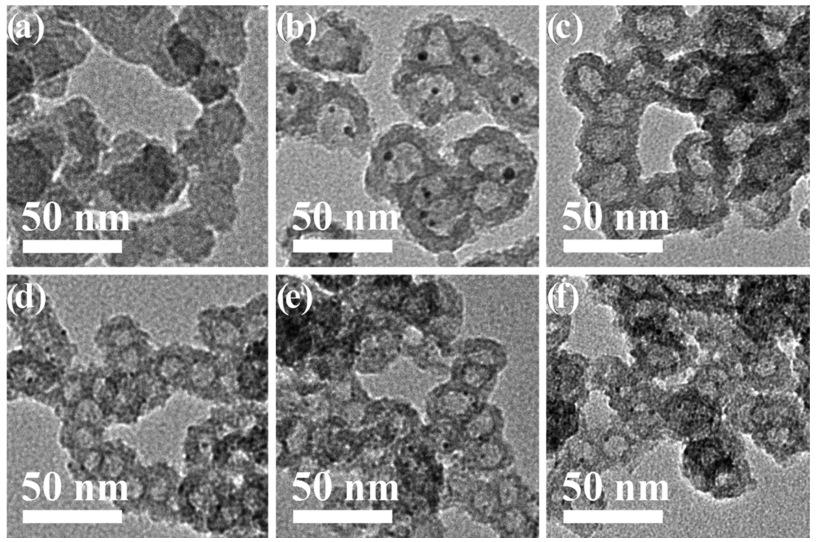

Figure 1. TEM images showing (a) silicified micelles of the precursors of $Pt_{0.77}Rh_1$@HMSNs (before calcination); (b) Pt@HMSNs; (c) Rh@HMSNs; (d) $Pt_{11.1}Rh_1$@HMSNs; (e) $Pt_{2.5}Rh_1$@HMSNs; and (f) $Pt_{0.77}Rh_1$@HMSNs. Scale bars are 50 nm. The materials in (b–f) are prepared by calcination at 500 °C and subsequent reduction by H_2 at 200 °C.

protection of mesoporous silica shells, the relatively large mesoporous channels (~8–10 nm), and the confinement effect of functional NPs inside hollow cavities, the catalytic efficiency and stability have been greatly improved.[29−31]

In this work, we extended the charge-driven template method to synthesize hollow mesoporous nanoreactors with encaged PtRh bimetallic NPs (PtRh@HMSNs) for hydrogenation of toluene to methyl cyclohexane. Scheme 1 presents the synthetic procedures for PtRh@HMSNs, which feature tiny PtRh NPs (~1–2 nm) in the ~11 nm hollow cavities of ~24 nm of mesoporous silica nanospheres. $Pt_{0.77}Rh_1$@HMSNs exhibit a high yield of >99% of methyl cyclohexane for toluene hydrogenation under the reaction conditions of 30 °C and 0.1 MPa of H_2, showing a much better performance than monometallic Pt@HMSNs and Rh@HMSNs and their physical mixtures. The catalytic enhancement of $Pt_{0.77}Rh_1$@HMSNs is ascribed to the Pt–Rh interaction and the confinement effect of functional PtRh bimetallic NPs inside hollow cavities.

2. RESULTS AND DISCUSSION

2.1. Synthesis and Characterization. In the synthesis, negatively charged coordination complex networks were formed by the coordination of L_3 and metal ions (Pt^{2+} and Rh^{3+}), which further combine with the positively charged diblock copolymer $P2MVP_{128}$-*b*-PEO_{477} to give metal-ion-containing core–shell-like micelles by electrostatic attraction. Hydrolysis of tetraethyl orthosilicate (TEOS) will deposit silica onto micelles to give silicified micelles. After calcination and reduction of silicified micelles, hollow mesoporous Pt_xRh_y@HMSNs are obtained. During the synthesis, pH values of the solution are the key parameters for the synthesis of such hollow mesoporous nanoreactors. Generally, lower pH values will protonate L_3 ligands (decreasing the coordination of metal ions and L_3 ligands), while higher pH values will favor deprotonation of L_3 ligands but will cause the formation of metal hydroxides. Therefore, a pH value of 4.15 is selected in this work.

Figure 1 presents transmission electron microscopy (TEM) images of various HMSNs. The silicified micelles in Figure 1a

https://dx.doi.org/10.1021/acsomega.0c06268
ACS Omega 2021, 6, 5846−5855

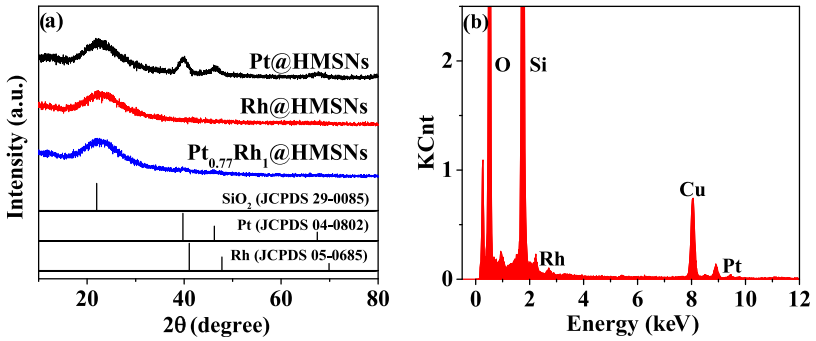

Figure 2. (a) XRD patterns of Pt@HMSNs, Rh@HMSNs, and $Pt_{0.77}Rh_1$@HMSNs; (b) EDS measurement of $Pt_{0.77}Rh_1$@HMSNs. All materials are prepared by calcination at 500 °C and subsequent reduction by H_2 at 200 °C.

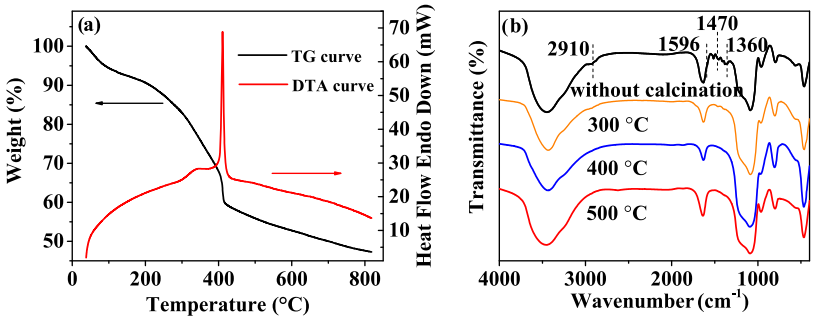

Figure 3. (a) TG/DTA curves of silicified precursors of $Pt_{0.77}Rh_1$@HMSNs (without calcination); (b) FT-IR spectra of silicified precursors of $Pt_{0.77}Rh_1$@HMSNs before and after calcination at various temperatures.

exhibit the structures of connected solid nanospheres, which consist of silica shells and metal-ion-containing micelles. As shown in Figure 1b–f, distinct hollow nanoreactors with small NPs inside their hollow cavities are observed due to the removal of organic components by calcination and reduction. Apparently, monometallic HMSNs exhibit relatively large hollow cavities and whole nanoreactors (Figure 1b,c). Moreover, the average size of inner NPs of Pt@HMSNs is larger than those of Rh@HMSNs and Pt_xRh_y@HMSNs. Figure S1 shows size analyses of various HMSNs. Pt@HMSNs and Rh@HMSNs (Figure S1b,c) demonstrate ∼17–22 nm hollow cavities and ∼31–37 nm whole nanoreactors, while bimetallic Pt_xRh_y@HMSNs (Figure S1d–f) present smaller hollow cavities/whole nanoreactors (∼11–12/∼24–25 nm), possibly due to the formation of smaller metal-ion-containing micelles by use of two metal ions. Figure S2 presents the size analyses of inner NPs of various HMSNs. The inner Pt particle sizes shown in Figure S2a are ∼3.7 nm, while the particle sizes of Rh and Pt_xRh_y NPs are ∼1–2 nm (Figure S2b–e), suggesting that the incorporation of Rh into Pt will decrease the particle size.

Figure 2a shows X-ray diffraction (XRD) patterns of Pt@HMSNs, Rh@HMSNs, and $Pt_{0.77}Rh_1$@HMSNs. The diffraction at ∼22 2θ degree is ascribed to SiO_2. As shown in Figure 2a, Pt@HMSNs show distinct fcc Pt diffractions, while those of Rh@HMSNs and $Pt_{0.77}Rh_1$@HMSNs present weak or even no obvious metal diffractions. These weak diffractions of Rh@HMSNs and $Pt_{0.77}Rh_1$@HMSNs are consistent with their extremely small sizes (∼1 nm, Figure S2b,e). Figure 2b presents the energy-dispersive spectroscopy (EDS) measurement of $Pt_{0.77}Rh_1$@HMSNs. The copresence of Rh and Pt in $Pt_{0.77}Rh_1$@HMSNs is confirmed. Moreover, inductively coupled plasma-atomic emission spectroscopy (ICP-OES) measurements of various HMSNs further confirm the copresence of Pt and Rh in $Pt_{0.77}Rh_1$@HMSNs (will discuss later).

H_2-temperature-programmed reduction (TPR) studies of $Pt_{0.77}Rh_1$@HMSNs calcined at 500 °C are shown in Figure S3a. Two distinct peaks centered at 85 and 356 °C are observed, where the former is assigned to the reduction of Rh_xO_y to metallic Rh and the latter can be ascribed to the reducibility of supports by H_2 spillover in the presence of Rh or the Rh_xO_y species having strong interaction with supports.[32−34] It is well known that metallic Pt is formed by calcination at high temperatures. Therefore, no reduction peak for Pt oxides is reasonable, which is also consistent with previous reports.[35,36] A previous study reported that PtRh alloys show (111) diffraction at ∼39.9 2θ degree,[37] which is very close to 39.7 2θ degree of Pt (111) diffraction. Because the inner NPs of $Pt_{0.77}Rh_1$@HMSNs are extremely small (∼1 nm), the PtRh alloy formation cannot be confirmed by XRD studies. Moreover, the $Pt_{0.77}Rh_1$ NPs are encaged inside hollow cavities; so, X-ray photoelectron spectroscopy (XPS) studies are also not applicable (shown in Figure S3b,c, high noise/signal ratios for Pt and Rh). The formation of bimetallic PtRh NPs can only be inferred from indirect evidence. As shown in Figure 2b, EDS measurements show the copresence of Pt and Rh in $Pt_{0.77}Rh_1$@HMSNs, confirming the incorporation of Pt and Rh into the HMSNs. Moreover, the size of inner NPs of $Pt_{0.77}Rh_1$@HMSNs is significantly smaller than those of Pt@HMSNs, suggesting the effect of Rh incorporation on particle sizes. Furthermore, $Pt_{0.77}Rh_1$@HMSNs show greatly enhanced catalytic performance relative to Rh@HMSNs, Pt@HMSNs, and their physical mixtures (will discuss later), suggesting the promoting effect of Pt on Rh (Pt@HMSNs show no observable activity). Therefore, it is speculated that the

https://dx.doi.org/10.1021/acsomega.0c06268
ACS Omega 2021, 6, 5846−5855

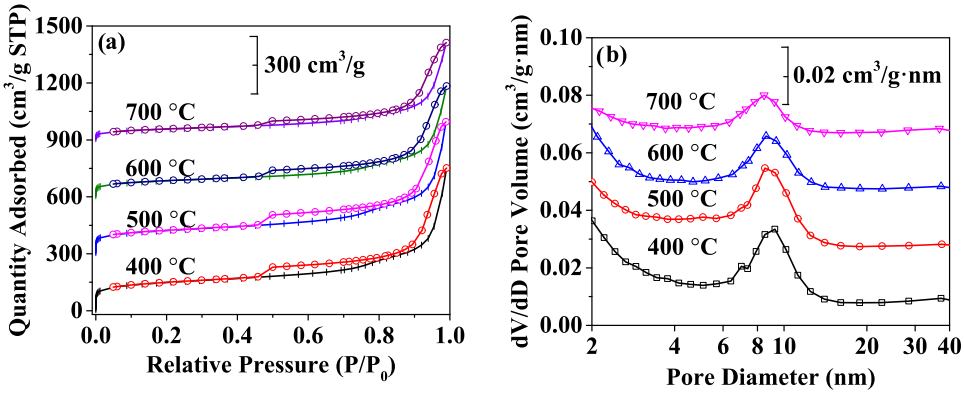

Figure 4. (a) N_2 adsorption−desorption isotherms of $Pt_{0.77}Rh_1$@HMSNs prepared by calcination at various temperatures and subsequent H_2 reduction at 200 °C; (b) their corresponding pore size distributions by the BJH method.

encaged NPs of $Pt_{0.77}Rh_1$@HMSNs are most likely bimetallic PtRh NPs.

Figure 3a shows thermogravimetry/differential thermal analysis (TG/DTA) curves of the precursors of $Pt_{0.77}Rh_1$@HMSNs (before calcination). The DTA curve has a sharp peak near 410 °C, indicating that the organic components are dramatically oxidized around this temperature. This sharp peak in the DTA curve is consistent with the obvious mass loss in the same temperature range in the TG curve. Figure 3b presents the Fourier transform infrared (FT-IR) spectra of $Pt_{0.77}Rh_1$@HMSNs calcined at different temperatures. As shown in the black spectrum, the peaks from 1360 to 1470 cm^{-1} are clearly visible and can be assigned to the in-plane bending vibration of the C−H bond,[38−41] while the peaks at 1596 and 2910 cm^{-1} are attributed to the asymmetric stretching vibration of carboxylic groups of L_3 ligands and methylene of polymer, respectively.[42−44] After calcination at 300 °C, the sample shows trace signals of the above-mentioned peaks (orange spectra), indicating incomplete removal of organic components at 300 °C. Although the sharp peak of the DTA curve is at 410 °C, it can be seen from the blue spectrum in Figure 3b that the organic components are completely removed after calcination at 400 °C for 3 h. Moreover, the spectrum calcined at 500 °C is the same as that at 400 °C, further confirming the complete removal of organic components by calcination at 400 °C for 3.0 h. Furthermore, the weight of $Pt_{0.77}Rh_1$@HMSNs calcined at 700 °C for 3.0 h is only 0.4% lower than that of $Pt_{0.77}Rh_1$@HMSNs calcined at 400 °C for 3.0 h, once again indicating a complete removal of organic components by calcination at 400 °C for 3.0 h.

Figure 4 shows the N_2 adsorption−desorption isotherms and pore size distributions of $Pt_{0.77}Rh_1$@HMSNs calcined at different temperatures and subsequently reduced at 200 °C by H_2. As shown in Figure 4a, type IV isotherms with characteristic hysteresis loops are obvious for all tested HMSNs, confirming the formation of mesopores.[40,45−47] The formation of aggregation voids between connected nanoreactors is proved by the sharp absorption at $\sim P/P_0$ of 0.9, and the enforced closures at $\sim P/P_0$ of 0.45 indicate the presence of hollow cavities.[45−47] Although the hysteresis loops become smaller with the increase of calcination temperature from 400 to 700 °C, the hysteresis loop is still visible at calcination of 700 °C. As shown in Figure S4, distinct hollow nanoreactors with extremely small NPs inside cavities are still observed even at the calcination temperature of 700 °C, which is consistent with its N_2 adsorption−desorption isotherms. Figure 4b shows the corresponding pore size distributions of $Pt_{0.77}Rh_1$@HMSNs, where mesoporous pores between 8 and 10 nm are observed. It is worth mentioning here that these relatively large mesoporous channels could facilitate the mass transfer for catalytic reactions.

Table 1 summarizes the textural properties of $Pt_{0.77}Rh_1$@HMSNs calcined at different temperatures and subsequently reduced at 200 °C by H_2. As the calcination temperature increases from 400 to 700 °C, the Brunauer−Emmett−Teller (BET) specific surface areas of $Pt_{0.77}Rh_1$@HMSNs decrease from 490.4 to 198.9 m^2/g, while pore volumes decrease from 0.65 to 0.41 cm^3/g in the same calcination temperature range, certainly due to the pore collapse at higher temperatures. The average pore sizes show a slight increase in the same calcination temperature range, due to the decrease of the number of micropores by sintering.

Table 1. Textural Properties of $Pt_{0.77}Rh_1$@HMSNs Prepared by Calcination at Various Temperatures and Subsequent H_2 Reduction at 200 °C

samples	S_{BET} (m^2/g)	pore volume (cm^3/g)[a]	average pore size (nm)[b]
$Pt_{0.77}Rh_1$@HMSNs-400 °C	490.4	0.65	16.3
$Pt_{0.77}Rh_1$@HMSNs-500 °C	409.4	0.59	16.0
$Pt_{0.77}Rh_1$@HMSNs-600 °C	285.7	0.48	17.9
$Pt_{0.77}Rh_1$@HMSNs-700 °C	198.9	0.41	18.8

[a]Pore volume is the single point adsorption total pore volume of pores. [b]verage pore size is the BJH adsorption average pore diameter.

2.2. Catalytic Hydrogenation of Toluene. The toluene hydrogenation reactions were carried out under the reaction conditions of 30 °C, 0.1 MPa of H_2, and organic solvents. Moreover, catalytic reactions were performed at a molar ratio of toluene/(Pt+Rh) of 200/1. Table 2 summarizes the actual Pt and Rh loadings of various Pt_xRh_y@HMSNs determined by ICP-OES. To keep the same molar ratio of toluene/(total metal) of 200/1, different weights of catalysts were used since their Pt and Rh loadings are different.

The influences of Pt/Rh ratios of Pt_xRh_y@HMSNs on their catalytic performance were investigated to correlate the relationship between Pt/Rh ratios and their catalytic activities. In this reaction, the selectivity for methyl cyclohexane is 100.0%. Therefore, the yield of methyl cyclohexane is used, which is the same as the toluene conversion. As shown in Figure 5a, monometallic Pt@HMSNs exhibit no obvious

https://dx.doi.org/10.1021/acsomega.0c06268
ACS Omega 2021, 6, 5846−5855

Table 2. The Actual Metal Loadings of Pt and Rh of Pt_xRh_y@HMSNs by ICP-OES

samples[a]	nominal Pt/Rh	Pt/Rh by ICP-OES	metal loadings (wt %)	
			Pt	Rh
Pt@HMSNs	N/A	N/A	3.8	N/A
$Pt_{11.1}Rh_1$@HMSNs	3/1	11.1/1	5.9	0.28
$Pt_{2.5}Rh_1$@HMSNs	1/1	2.5/1	1.7	0.35
$Pt_{0.77}Rh_1$@HMSNs	1/3	0.77/1	1.2	0.82
Rh@HMSNs	N/A	N/A	N/A	1.6

[a]All materials were calcined at 500 °C and subsequently reduced at 200 °C.

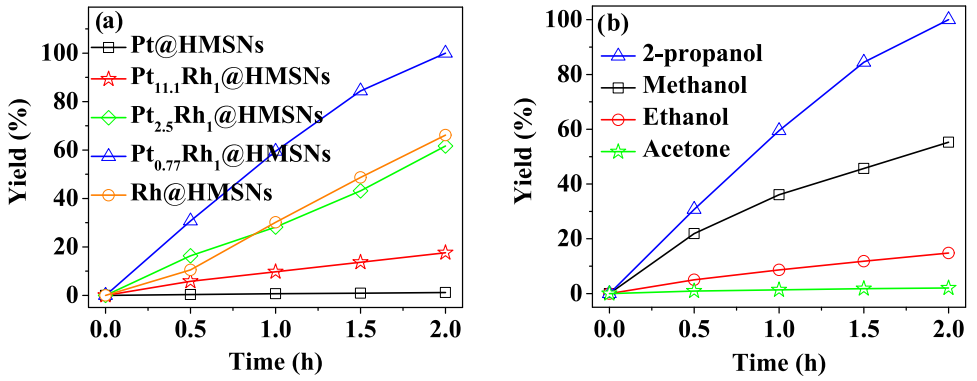

Figure 5. (a) Effects of the Pt/Rh molar ratios on methyl cyclohexane yields over Pt_xRh_y@HMSNs; (b) effects of solvents on the catalytic performance over $Pt_{0.77}Rh_1$@HMSNs. All catalysts were calcined at 500 °C and reduced by H_2 at 200 °C. Reaction conditions: toluene, 32.9 μL; toluene/(Pt+Rh) molar ratio, 200/1; solvents 10.0 mL, 2-propanol for (a); H_2, 0.1 MPa; reaction temperature, 30 °C; and speed of agitation, 500 rpm.

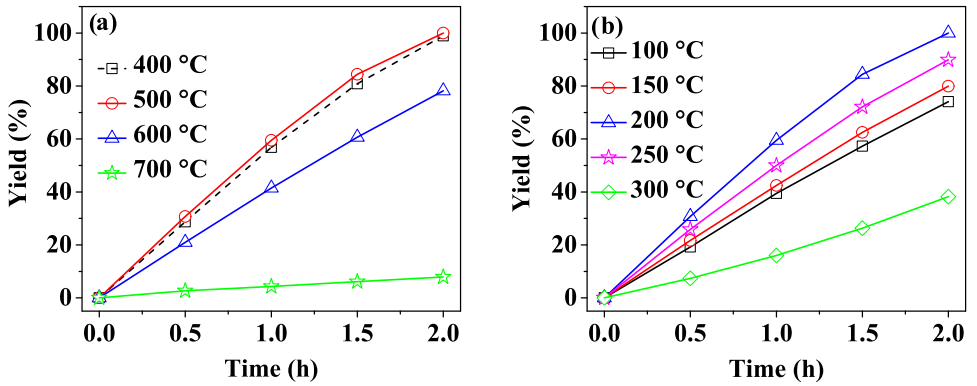

Figure 6. Effects of (a) calcination temperatures and (b) reduction temperatures of $Pt_{0.77}Rh_1$@HMSNs on methyl cyclohexane yields over $Pt_{0.77}Rh_1$@HMSNs. Reduction at 200 °C for (a) and calcination at 500 °C for (b). Reaction conditions: toluene, 32.9 μL; toluene/(Pt+Rh) molar ratio, 200/1; 2-propanol, 10.0 mL; H_2, 0.1 MPa; reaction temperature, 30 °C; and speed of agitation, 500 rpm.

activity (1.2% of methyl cyclohexane yield) for toluene hydrogenation at the selected reaction conditions, which is consistent with a previous work.[17] In contrast, Rh@HMSNs achieve a yield of 66.2% at 2.0 h. With the constant total metal atoms, $Pt_{11.1}Rh_1$@HMSNs and $Pt_{2.5}Rh_1$@HMSNs achieve yields of 17.6 and 61.7% at 2.0 h, respectively, which are lower than that of Rh@HMSNs. However, $Pt_{0.77}Rh_1$@HMSNs attain 100.0% of yield at 2.0 h, showing a much better catalytic performance than that of Rh@HMSNs.

Under the selected reaction conditions, monometallic Pt@HMSNs show no obvious activity, while monometallic Rh@HMSNs demonstrate a good activity, confirming that Rh is a better catalyst than Pt for hydrogenation of toluene. With the same total (Pt+Rh) atoms, the physical mixture of Pt@HMSNs and Rh@HMSNs (the molar ratio of Pt/Rh of 0.77/1) approaches only 18.0% of yield at 2.0 h (Figure S5a), while proper incorporation of Pt atoms into Rh atoms at the Pt/Rh ratio of 0.77/1 results in even better catalytic performance than monometallic Rh@HMSNs, indicating the promoting effect of Pt on Rh. The interaction between Pt and Rh could adjust the electronic state of Rh and thereby improve the catalytic activity. Moreover, the addition of too much Pt into Rh ($Pt_{11.1}Rh_1$@HMSNs) results in the decrease of the activity, possibly due to the excessive dilution of the Rh surface with Pt atoms. Furthermore, the commercial silica-supported $Pt_{0.83}Rh_1/SiO_2$ catalysts (nominal Pt/Rh ratio of 0.77/1), prepared by a typical impregnation method and same treatments, show a yield of 8.7% at 2.0 h (Figure S5a), which is much lower than that of $Pt_{0.77}Rh_1$@HMSNs. Figure S5b shows TEM images of $Pt_{0.83}Rh_1/SiO_2$, where ~3.0 nm particles are observed and are larger than those inner NPs of $Pt_{0.77}Rh_1$@HMSNs. It is concluded that $Pt_{0.77}Rh_1$@HMSNs

https://dx.doi.org/10.1021/acsomega.0c06268
ACS Omega 2021, 6, 5846−5855

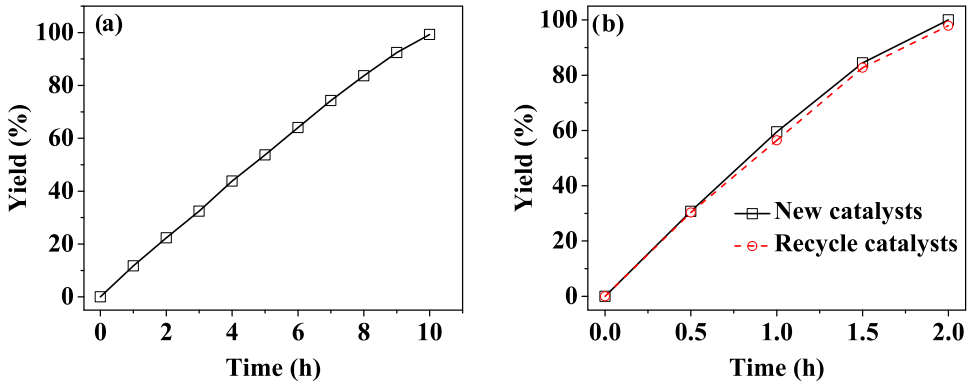

Figure 7. (a) Toluene hydrogenation over $Pt_{0.77}Rh_1$@HMSNs at a high toluene/(Pt+Rh) ratio of 1000/1; (b) toluene hydrogenation over the recovered $Pt_{0.77}Rh_1$@HMSNs at a toluene/(Pt+Rh) ratio of 200/1. Reaction conditions: toluene, 164.5 μL for (a) and 32.9 μL for (b); 2-propanol, 20.0 mL for (a) and 10.0 mL for (b); H_2, 0.1 MPa; reaction temperature, 30 °C; and speed of agitation, 500 rpm. $Pt_{0.77}Rh_1$@HMSNs are prepared under calcination at 500 °C and subsequent H_2 reduction at 200 °C.

possess smaller active NPs due to the coordination method employed and show much better performance than their conventional silica-supported counterparts. In this work, $Pt_{0.77}Rh_1$@HMSNs were selected for further studies since they exhibit the best toluene hydrogenation activity.

It is well known that solvents can provide a unique reaction environment for catalytic reactions to happen. Previous studies have reported that a solvent could influence the dispersion of solid catalysts[48−50] and also the H_2 solubility.[51−54] It is mentioned that no obvious reactions occur with the selected solvents in the blank experiments (only solvents, H_2 and catalysts). As indicated in Figure 5b, the solvents indeed dramatically influence the hydrogenation activity of $Pt_{0.77}Rh_1$@HMSNs. Using acetone, ethanol, and methanol as solvents resulted in only 2.0, 14.8, and 55.3% of yields, respectively, while 2-propanol showed 100.0% of yield for toluene hydrogenation. The detailed explanation for solvent effects is unclear and may be related to the H_2 solubility and/or the dispersion of the catalysts. A previous study has reported that 2-propanol possibly acts as a bridge for the hydrogen exchange process with H_2 or reactants, thereby enhancing the catalytic performance.[55] In this study, 2-propanol was selected for further studies since it exhibits the best performance.

Figure 6a shows the effects of calcination temperatures of $Pt_{0.77}Rh_1$@HMSNs on their catalytic performance. The subsequent H_2 reduction temperature is 200 °C for all $Pt_{0.77}Rh_1$@HMSNs with different calcination temperatures. As shown in Figure 6a, the yields increased from 98.9 to 100.0% at 2.0 h with the increase of calcination temperature from 400 to 500 °C. With further increase of calcination temperatures, the yields decreased to 78.1% at 2.0 h with the calcination at 600 °C and dramatically decreased to 7.8% at 2.0 h with the calcination at 700 °C. As shown in Figure S4, TEM images show a small change in particle sizes of inner NPs for all $Pt_{0.77}Rh_1$@HMSNs calcined at 400−700 °C, suggesting that the size change of inner NPs is not the main reason for the difference among these catalysts. The change in texture properties may be the main reason for the degradation of the catalytic performance of $Pt_{0.77}Rh_1$@HMSNs with a calcination temperature higher than 500 °C. As illustrated in Table 1, the specific surface areas/pore volumes of $Pt_{0.77}Rh_1$@HMSNS dramatically decrease from 409.4 m^2/g/0.59 cm^3/g with 500 °C calcination to 285.7 m^2/g/0.48 cm^3/g with 600 °C calcination, resulting in the performance degradation. In addition, it is speculated that the change of surface composition of PtRh bimetallic NPs induced by calcination at different temperatures may also influence their catalytic performance. Among various calcination temperatures, calcination at 500 °C can achieve the best catalytic performance for toluene hydrogenation.

Figure 6b shows the effects of reduction temperatures of $Pt_{0.77}Rh_1$@HMSNs on their catalytic performance. All $Pt_{0.77}Rh_1$@HMSNs with different reduction temperatures are previously calcined at 500 °C. As shown in Figure 6b, reduction at 200 °C gives the best performance for toluene hydrogenation. Figure S6 shows TEM images of $Pt_{0.77}Rh_1$@HMSNs with different reduction temperatures. No significant change in particle size is observed, suggesting that the particle size change induced by reductions at different temperatures is not the main reason for the performance difference. Therefore, we speculate that the lower reduction temperature at 100 °C may not form PtRh bimetallic alloy structures. Currently, the reason for the worse performance at higher reduction temperatures ≥250 °C is unclear, possibly due to an unsuitable metal−support interaction at higher reduction temperatures. Moreover, the influence of the weights of $Pt_{0.77}Rh_1$@HMSNs on their catalytic performance was studied. As shown in Figure S7, the yields of methyl cyclohexane at 2.0 h of reaction time first increased with the increase of catalyst weights and attained 100.0% at a reaction time of 1.5 h when the catalyst weight was 14.2 mg (toluene/(Rh + Pt)-154/1). The increase of yields with the increase of catalyst weights is apparently due to the larger amount of catalyst used in the reaction.

The catalytic stability of $Pt_{0.77}Rh_1$@HMSNs with 500 °C calcination and reduction at 200 °C was investigated, and the results are shown in Figure 7. To reduce the loss of the catalyst during the recovery process, the stability experiments were performed under a high toluene/(Pt+Rh) molar ratio of 1000/1 that is 5 times higher than that of the normal tests. After the experiment with a toluene/(Pt+Rh) ratio of 1000/1, the catalysts were collected by centrifugation, washing, and drying for a subsequent normal test at a toluene/(Pt+Rh) ratio of 200/1. Based on the amount of reactants treated, the overall experiments are equal to six cycles of normal experiments, and the reaction time is equal to total reaction time in six typical cycle experiments. As shown in Figure 7a, the hydrogenation reaction at a toluene/(Pt+Rh) ratio of 1000/1 achieves 99.3% of yield at 10.0 h. The turnover frequency (moles of products

https://dx.doi.org/10.1021/acsomega.0c06268
ACS Omega 2021, 6, 5846−5855

per total molar (Pt+Rh) atoms per hour, TOF, h^{-1}) is 99.3 h^{-1} at a yield of 99.3% (achieved at 10.0 h), which is very close to the TOF of 100 h^{-1} of the fresh catalyst at 100.0% of yield (achieved at 2.0 h, Figure 5a, blue curve). As shown in Figure 7b, after having treated five times with reactants, the recovered $Pt_{0.77}Rh_1$@HMSNs exhibit a nearly same performance with a 97.9% of yield at 2.0 h as that of the fresh catalysts, showing a superior catalytic stability. This excellent catalytic stability could have originated from their unique structures.

Previous studies have reported the application of hollow mesoporous nanoreactors in various reactions, and a significantly enhanced catalytic performance has been achieved due to the protection and confinement effects of hollow mesoporous nanoreactors.[56−59] By encaging PtRh NPs into the hollow cavities of mesoporous silica nanoreactors, we can expect increased catalytic stability due to the protection of silica shells. Indeed, no detectable metal in the reaction solution is observed by ICP-OES, confirming the protection of silica shells for inner NPs. Moreover, PtRh@HMSNs have relatively large mesoporous channels with mesopore sizes around 8−10 nm and thereby facilitate the mass transportation during reactions. Furthermore, we speculate that the residence of PtRh NPs inside hollow cavities could increase the collision times between reactants and PtRh NPs, thus enhancing their catalytic efficiency.

3. CONCLUSIONS

In this study, using metal-ion-containing polymer micelles as templates, bimetallic PtRh NP-encaged hollow mesoporous silica nanoreactors are prepared, which feature ∼1−2 nm tiny PtRh NPs in ∼11 nm hollow cavities of nanoreactors. The synthesized $Pt_{0.77}Rh_1$@HMSNs show a much better toluene hydrogenation activity than monometallic Pt@HMSNs and Rh@HMSNs and their physical mixtures. Under reaction conditions of 30 °C, 0.1 MPa, and a toluene/(Pt+Rh) ratio of 200/1, 100.0% of methyl cyclohexane yield is achieved for toluene hydrogenation at a reaction time of 2.0 h. The enhanced catalytic performance of $Pt_{0.77}Rh_1$@HMSNs is ascribed to the protection effect of silica shells and the confinement effect of functional NPs inside hollow cavities. We believe that such bimetallic NP-encaged hollow mesoporous nanoreactors may find more applications in heterogeneous catalytic reactions, and the synthetic method could be extended to other systems.

4. EXPERIMENTAL SECTION

4.1. Chemicals. Nitric acid (HNO_3, 65−68%) and sodium hydroxide (NaOH, ≥96.0%) were purchased from Shanghai Chemical Reagent Company. Toluene (C_7H_8, ≥99.5%) and acetone (CH_3COCH_3, ≥99.5%) were purchased from General Reagents. Ethanol (AR), methyl cyclohexane (C_7H_{14}, 99.0%), and tetrahydrofuran (C_4H_8O, ≥99.0%) were purchased from Aladdin. Potassium hexachlororhodate (K_3RhCl_6, Rh ≥23.3%) was purchased from Macklin. Methanol (CH_3OH, ≥99.5%) was purchased from Sinopharm Chemical Reagent Co., Ltd., while potassium tetrachloroplatinate (K_2PtCl_4, Pt ≥46.4%) and 2-propanol (C_3H_8O, ≥99.5%) were purchased from AI LAN (Shanghai) Chemical Technology Ltd. and Sun Chemical Technology (Shanghai) Co., Ltd., respectively. $P2MVP_{128}$-*b*-PEO_{477} (M_w/M_n = 1.1, M_w = 34.5k) was synthesized according to a previously reported work.[60] The positively charged diblock copolymer was obtained by quaternization of $P2MVP_{128}$-*b*-PEO_{477} by methyl iodide, and the quaternization level is ∼90%. 1,3,5-Tris(2,6-dicarboxypyridin-4-yloxymethyl) benzene (L_3) was synthesized in based on a previous study.[61] All reagents were used as received.

4.2. Syntheses of Bimetallic Pt_xRh_y@HMSNs and Monometallic Pt@HMSNs and Rh@HMSNs. In the syntheses of Pt_xRh_y@HMSNs, the nomenclature of Pt_xRh_y@HMSNs is based on the real molar ratios of Pt/Rh determined by ICP-OES. The nominal molar ratios of Pt/Rh are significantly larger than the real ratios of Pt/Rh determined by ICP-OES due to the weak coordination between Rh ions and L_3 ligands. Only a small percentage of Rh ions are incorporated into HMSNs, and the uncoordinated Rh ions are left in the solution and will be separated from HMSNs by centrifugation. According to our previous work,[62] the synthesis of Rh@HMSNs will result in low Rh loading with extremely small Rh nanoclusters inside hollow cavities.

4.2.1. $Pt_{0.77}Rh_1$@HMSNs. The synthetic procedures are modified from our previous work.[63] In a typical synthesis of $Pt_{0.77}Rh_1$@HMSNs, 1080 μL of 5.0 mM K_3RhCl_6 aqueous solution, 360 μL of 5.0 mM K_2PtCl_4 aqueous solution (nominal molar ratio of Pt/Rh of 1/3), 1980 μL of 0.087 mM quaternized $P2MVP_{128}$-*b*-PEO_{477} aqueous solution, 1320 μL of 5.0 mM L_3 aqueous solution, and 35.26 mL of deionized water were mixed in a 50 mL beaker with magnetic stirring at 200 rpm. The pH value of the solution was adjusted to about 4.15 by diluted NaOH or HNO_3 aqueous solution. Subsequently, 290 μL of TEOS was added into the above solution. The obtained mixture was stirred for 48 h to allow the deposition of silica onto the micelles (white precipitates will appear during 24−48 h). The system was left untouched for 1 more day. Afterward, the white precipitates were collected by centrifugation and washing several times with water and ethanol successively. The collected white precipitates were dried in an oven at 55 °C for 12 h, then calcined at 400−700 °C in a muffle furnace for 3 h, and subsequently reduced in a tube furnace with H_2 at 200 °C for 3 h to obtain $Pt_{0.77}Rh_1$@HMSNs.

4.2.2. $Pt_{11.1}Rh_1$@HMSNs. The synthetic procedures for $Pt_{11.1}Rh_1$@HMSNs were the same as that of $Pt_{0.77}Rh_1$@HMSNs except that 360 μL of 5.0 mM K_3RhCl_6 aqueous solution, 1080 μL of 5.0 mM K_2PtCl_4 aqueous solution (nominal ratios of Pt/Rh of 3/1), 1620 μL of 0.087 mM quaternized $P2MVP_{128}$-*b*-PEO_{477} aqueous solution, 1080 μL of 5.0 mM L_3 aqueous solution, and 35.86 mL of deionized water were used.

4.2.3. $Pt_{2.5}Rh_1$@HMSNs. The synthetic procedures for $Pt_{2.5}Rh_1$@HMSNs were the same as that of $Pt_{0.77}Rh_1$@HMSNs except that 720 μL of 5.0 mM K_3RhCl_6 aqueous solution, 720 μL of 5.0 mM K_2PtCl_4 aqueous solution (nominal ratios of Pt/Rh of 1/1), 1800 μL of 0.087 mM quaternized $P2MVP_{128}$-*b*-PEO_{477} aqueous solution, 1200 μL of 5.0 mM L_3 aqueous solution, and 35.56 mL of deionized water were used.

4.2.4. Pt@HMSNs. The synthetic procedures for Pt@HMSNs were the same as that of $Pt_{0.77}Rh_1$@HMSNs except that 720 μL of 5.0 mM K_2PtCl_4 aqueous solution, 1440 μL of 0.087 mM quaternized $P2MVP_{128}$-*b*-PEO_{477} aqueous solution, 960 μL of 5.0 mM L_3 aqueous solution, and 36.88 mL of deionized water were used.

4.2.5. Rh@HMSNs. The synthetic procedures for Rh@HMSNs were the same as that of $Pt_{0.77}Rh_1$@HMSNs except that 1440 μL of 5.0 mM K_3RhCl_6 aqueous solution, 2160 μL of

https://dx.doi.org/10.1021/acsomega.0c06268
ACS Omega 2021, 6, 5846−5855

0.087 mM quaternized $P2MVP_{128}$-*b*-PEO_{477} aqueous solution, 1440 μL of 5.0 mM L_3 aqueous solution, and 34.96 mL of deionized water were used.

4.3. Catalyst Characterization. A Bruker D8 advanced diffractometer with Cu Kα radiation was used to obtain X-ray diffraction (XRD) patterns of various materials in the 2θ range from 10 to 80°. The images of transmission electron microscopy (TEM) were obtained using a JEM-2100 transmission electron microscope operated at 200 kV. A PE Optima 2100DV inductively coupled plasma emission spectrometer (ICP-OES) was used to analyze the actual Pt and Rh loadings in different HMSNs. A Micromeritics ASAP-2020 automatic specific surface area and porous physical adsorption analyzer was used to obtain the Brunauer−Emmett−Teller (BET) specific surface area, pore size distribution, and adsorption/desorption isotherms of various materials by N_2 adsorption at 77 K. A Nicolet Nexus 670 spectrophotometer was used to obtain Fourier transform infrared (FT-IR) spectra of HMSNs before and after calcination. A PerkinElmer Pyris Diamond thermogravimetric analyzer (TG/DTA) was used to investigate the thermal property of the samples in the temperature range from 40 to 1200 °C at a heating rate of 10 °C/min with a gas flow rate of 100 mL/min in an air atmosphere.

4.4. Catalytic Activity Measurement. All catalytic reactions were carried out in a 25 mL three-neck round-bottomed flask under atmospheric H_2 pressure. As an example, 10.9 mg of $Pt_{0.77}Rh_1$@HMSNs (Pt-6.70×10^{-4} mmol; Rh-8.69×10^{-4} mmol) and 10.0 mL of 2-propanol solution containing 32.9 μL of toluene (0.31 mmol, the molar ratio of toluene/(Pt+Rh) was 200/1) were charged into a 25 mL three-neck round-bottomed flask under magnetic stirring at 500 rpm. Catalytic reactions were carried out under H_2 bubbling at 30 °C and 0.1 MPa of H_2. The catalytic products were analyzed by gas chromatography (GC) with a flame ionization detector (FID). The quantification of components is based on relative response factors of components and their surface areas in GC. After hydrogenation, the product samples were first analyzed by GC to obtain relative surface areas of components, and then known amount of toluene or methyl cyclohexane was added to the samples as the external standards to obtain the corresponding GC chromatograms. Based on the relative response factors of components, and GC chromatograms of samples and samples with a known amount of reactants or main products, reactant conversions and main product selectivity can be accurately calculated.

■ ASSOCIATED CONTENT

Supporting Information

The Supporting Information is available free of charge at https://pubs.acs.org/doi/10.1021/acsomega.0c06268.

Further materials characterizations, size analysis and catalytic reactions (PDF)

■ AUTHOR INFORMATION

Corresponding Author

Shenghu Zhou − *Shanghai Key Laboratory of Multiphase Materials Chemical Engineering, School of Chemical Engineering, East China University of Science and Technology, Shanghai 200237, P. R. China;* orcid.org/0000-0002-8203-6546; Email: zhoushenghu@ecust.edu.cn; Fax: (+86) 21-64253159

Authors

Kaijie Li − *Shanghai Key Laboratory of Multiphase Materials Chemical Engineering, School of Chemical Engineering, East China University of Science and Technology, Shanghai 200237, P. R. China*

Heliang An − *Shanghai Key Laboratory of Multiphase Materials Chemical Engineering, School of Chemical Engineering, East China University of Science and Technology, Shanghai 200237, P. R. China*

Peijian Yan − *Shanghai Key Laboratory of Multiphase Materials Chemical Engineering, School of Chemical Engineering, East China University of Science and Technology, Shanghai 200237, P. R. China*

Caoping Yang − *Shanghai Key Laboratory of Multiphase Materials Chemical Engineering, School of Chemical Engineering, East China University of Science and Technology, Shanghai 200237, P. R. China*

Tao Xiao − *Shanghai Key Laboratory of Multiphase Materials Chemical Engineering, School of Chemical Engineering, East China University of Science and Technology, Shanghai 200237, P. R. China*

Junyou Wang − *Shanghai Key Laboratory of Multiphase Materials Chemical Engineering, School of Chemical Engineering, East China University of Science and Technology, Shanghai 200237, P. R. China;* orcid.org/0000-0002-4693-850X

Complete contact information is available at: https://pubs.acs.org/10.1021/acsomega.0c06268

Author Contributions

†K.L. and H.A. contributed equally to this work.

Notes

The authors declare no competing financial interest.

■ ACKNOWLEDGMENTS

S.Z. thanks the National Natural Science Foundation of China for financial support (Grant Nos. 22078099 and 21776090), and this work is also partially supported by the Natural Science Foundation of Shanghai (Grant No. 17ZR1440500)

■ REFERENCES

(1) Hosseini, S. E.; Wahid, M. A. Hydrogen from solar energy, a clean energy carrier from a sustainable source of energy. *Int. J. Energy Res.* **2020**, *44*, 4110−4131.

(2) Abdin, Z.; Zafaranloo, A.; Rafiee, A.; Mérida, W.; Lipiński, W.; Khalilpour, K. R. Hydrogen as an energy vector. *Renewable Sustainable Energy Rev.* **2020**, *120*, No. 109620.

(3) Alhumaidan, F.; Cresswell, D.; Garforth, A. Hydrogen Storage in Liquid Organic Hydride: Producing Hydrogen Catalytically from Methylcyclohexane. *Energy Fuels* **2011**, *25*, 4217−4234.

(4) Hu, P.; Ben-David, Y.; Milstein, D. Rechargeable Hydrogen Storage System Based on the Dehydrogenative Coupling of Ethylenediamine with Ethanol. *Angew. Chem., Int. Ed.* **2016**, *55*, 1061−1064.

(5) Latroche, M.; Surblé, S.; Serre, C.; Mellot-Draznieks, C.; Llewellyn, P. L.; Lee, J.; Chang, J.; Jhung, S. H.; Férey, G. Hydrogen Storage in the Giant-Pore Metal-Organic Frameworks MIL-100 and MIL-101. *Angew. Chem., Int. Ed.* **2006**, *45*, 8227−8231.

(6) Rosi, N. L.; Eckert, J.; Eddaoudi, M.; Vodak, D. T.; Kim, J.; O'Keeffe, M.; Yaghi, O. M. Hydrogen Storage in Microporous Metal-Organic Frameworks. *Science* **2003**, *300*, 1127−1129.

(7) Bakhshi, F.; Farhadian, N. Co-doped graphene sheets as a novel adsorbent for hydrogen storage: DFT and DFT-D3 correction dispersion study. *Int. J. Hydrogen Energy* **2018**, *43*, 8355−8364.

(8) Schneemann, A.; White, J. L.; Kang, S.; Jeong, S.; Wan, L. F.; Cho, E. S.; Heo, T. W.; Prendergast, D.; Urban, J. J.; Wood, B. C.; Allendorf, M. D.; Stavila, V. Nanostructured Metal Hydrides for Hydrogen Storage. *Chem. Rev.* **2018**, *118*, 10775−10839.
(9) Belkova, N. V.; Epstein, L. M.; Filippov, O. A.; Shubina, E. S. Hydrogen and Dihydrogen Bonds in the Reactions of Metal Hydrides. *Chem. Rev.* **2016**, *116*, 8545−8587.
(10) Rossin, A.; Peruzzini, M. Ammonia-Borane and Amine-Borane Dehydrogenation Mediated by Complex Metal Hydrides. *Chem. Rev.* **2016**, *116*, 8848−8872.
(11) Patil, S. P.; Bindwal, A. B.; Pakade, Y. B.; Biniwale, R. B. On H_2 supply through liquid organic hydrides-Effect of functional groups. *Int. J. Hydrogen Energy* **2017**, *42*, 16214−16224.
(12) Mu, X.; Meng, J.; Li, Z.; Kou, Y. Rhodium Nanoparticles Stabilized by Ionic Copolymers in Ionic Liquids: Long Lifetime Nanocluster Catalysts for Benzene Hydrogenation. *J. Am. Chem. Soc.* **2005**, *127*, 9694−9695.
(13) Pélisson, C.-H.; Denicourt-Nowicki, A.; Roucoux, A. Magnetically Retrievable Rh(0) Nanocomposite as Relevant Catalyst for Mild Hydrogenation of Functionalized Arenes in Water. *ACS Sustainable Chem. Eng.* **2016**, *4*, 1834−1839.
(14) Nasiruzzaman Shaikh, M.; Aziz, M. A.; Kalanthoden, A. N.; Helal, A.; Hakeem, A. S.; Bououdina, M. Facile hydrogenation of N-heteroarenes by magnetic nanoparticle-supported sub-nanometric Rh catalysts in aqueous medium. *Catal. Sci. Technol.* **2018**, *8*, 4709−4717.
(15) Sugiura, Y.; Nagatsuka, T.; Kubo, K.; Hirano, Y.; Sekine, Y.; et al. Dehydrogenation of Methylcyclohexane over Pt/TiO_2-Al_2O_3 Catalysts. *Chem. Lett.* **2017**, *46*, 1601−1604.
(16) Atsumi, R.; Kobayashi, K.; Xieli, C.; Nanba, T.; Matsumoto, H.; Matsuda, K.; Tsujimura, T. Effects of steam on toluene hydrogenation over a Ni catalyst. *Appl. Catal., A* **2020**, *590*, No. 117374.
(17) Dehm, N. A.; Zhang, X.; Buriak, J. M. Screening of Bimetallic Heterogeneous Nanoparticle Catalysts for Arene Hydrogenation Activity under Ambient Conditions. *Inorg. Chem.* **2010**, *49*, 2706−2714.
(18) Maximov, A.; Zolotukhina, A.; Kulikov, L.; Kardasheva, Y.; Karakhanov, E. Ruthenium catalysts based on mesoporous aromatic frameworks for the hydrogenation of arenes. *React. Kinet. Mech. Catal.* **2016**, *117*, 729−743.
(19) Zahmakıran, M.; Tonbul, Y.; Özkar, S. Ruthenium(0) Nanoclusters Stabilized by a Nanozeolite Framework: Isolable, Reusable, and Green Catalyst for the Hydrogenation of Neat Aromatics under Mild Conditions with the Unprecedented Catalytic Activity and Lifetime. *J. Am. Chem. Soc.* **2010**, *132*, 6541−6549.
(20) Snelders, D. J. M.; Yan, N.; Gan, W.; Laurenczy, G.; Dyson, P. J. Tuning the Chemoselectivity of Rh Nanoparticle Catalysts by Site-Selective Poisoning with Phosphine Ligands: The Hydrogenation of Functionalized Aromatic Compounds. *ACS Catal.* **2012**, *2*, 201−207.
(21) Giannoccaro, P.; Gargano, M.; Fanizzi, A.; Ferragina, C.; Aresta, M. Rh-ions and Rh-complexes intercalated in γ-titanium or γ-zirconium hydrogen phosphate as highly efficient catalysts for arene hydrogenation. *Appl. Catal., A* **2005**, *284*, 77−83.
(22) Miyamura, H.; Suzuki, A.; Yasukawa, T.; Kobayashi, S. Polysilane-Immobilized Rh-Pt Bimetallic Nanoparticles as Powerful Arene Hydrogenation Catalysts: Synthesis, Reactions under Batch and Flow Conditions and Reaction Mechanism. *J. Am. Chem. Soc.* **2018**, *140*, 11325−11334.
(23) Lin, R.; Ma, X.; Cheong, W.; Zhang, C.; Zhu, W.; Pei, J.; Zhang, K.; Wang, B.; Liang, S.; Liu, Y.; et al. PdAg bimetallic electrocatalyst for highly selective reduction of CO_2 with low COOH* formation energy and facile CO desorption. *Nano Res.* **2019**, *12*, 2866−2871.
(24) Wen, J.; Chen, Y.; Ji, S.; Zhang, J.; Wang, D.; Li, Y. Metal-organic frameworks-derived nitrogen-doped carbon supported nanostructured PtNi catalyst for enhanced hydrosilylation of 1-octene. *Nano Res.* **2019**, *12*, 2584−2588.
(25) Liu, J.; Yang, Q.; Zhang, L.; Yang, H.; Gao, J.; Li, C. Organic-Inorganic Hybrid Hollow Nanospheres with Microwindows on the Shell. *Chem. Mater.* **2008**, *20*, 4268−4275.
(26) Ren, X.; Guo, M.; Li, H.; Li, C.; Yu, L.; Liu, J.; Yang, Q. Microenvironment Engineering of Ruthenium Nanoparticles Incorporated into Silica Nanoreactors for Enhanced Hydrogenations. *Angew. Chem., Int. Ed.* **2019**, *58*, 14483−14488.
(27) Tian, H.; Zhao, J.; Wang, X.; Wang, L.; Liu, H.; Wang, G.; Huang, J.; Liu, J.; Lu, G. Q. Construction of hollow mesoporous silica nanoreactors for enhanced photo-oxidations over Au-Pt catalysts. *Natl. Sci. Rev.* **2020**, *7*, 1647−1655.
(28) Joo, S. H.; Park, J. Y.; Tsung, C.; Yamada, Y.; Yang, P.; Somorjai, G. A. Thermally stable Pt/mesoporous silica core-shell nanocatalysts for high-temperature reactions. *Nat. Mater.* **2009**, *8*, 126−131.
(29) Ding, S.; Chen, J. S.; Qi, G.; Duan, X.; Wang, Z.; Giannelis, E. P.; Archer, L. A.; Lou, X. W. Formation of SnO_2 Hollow Nanospheres inside Mesoporous Silica Nanoreactors. *J. Am. Chem. Soc.* **2011**, *133*, 21−23.
(30) Fang, X.; Liu, Z.; Hsieh, M.; Chen, M.; Liu, P.; Chen, C.; Zheng, N. Hollow Mesoporous Aluminosilica Spheres with Perpendicular Pore Channels as Catalytic Nanoreactors. *ACS Nano* **2012**, *6*, 4434−4444.
(31) Li, X.; Li, J. L.; Wang, Y.; Cai, T. Fabrication of Smart Hybrid Nanoreactors from Platinum Nanodendrites Encapsulating in Hyperbranched Polyglycerol Hollow Shells. *ACS Appl. Nano Mater.* **2018**, *1*, 2559−2566.
(32) Karatzas, X.; Jansson, K.; González, A.; Dawody, J.; Pettersson, L. J. Autothermal reforming of low-sulfur diesel over bimetallic RhPt supported on Al_2O_3, CeO_2-ZrO_2, SiO_2 and TiO_2. *Appl. Catal., B* **2011**, *106*, 476−487.
(33) Kaila, R. K.; Gutierrez, A.; Slioor, R.; Kemell, M.; Leskela, M.; Krause, A. O. I. Zirconia-supported bimetallic RhPt catalysts: Characterization and testing in autothermal reforming of simulated gasoline. *Appl. Catal., B* **2008**, *84*, 223−232.
(34) Karatzas, X.; Jansson, K.; Dawody, J.; Lanza, R.; Pettersson, L. J. Microemulsion and incipient wetness prepared Rh-based catalyst for diesel reforming. *Catal. Today* **2011**, *175*, 515−523.
(35) Liu, M.; Tang, W.; Xie, Z.; Yu, H.; Yin, H.; Xu, Y.; Zhao, S.; Zhou, S. Design of Highly Efficient Pt-SnO_2 Hydrogenation Nanocatalysts using Pt@Sn Core-Shell Nanoparticles. *ACS Catal.* **2017**, *7*, 1583−1591.
(36) Wang, X.; Yu, H.; Hua, D.; Zhou, S. Enhanced Catalytic Hydrogenation Activity and Selectivity of Pt-$MxOy/Al_2O_3$ (M = Ni, Fe, Co) Heteroaggregate Catalysts by in Situ Transformation of PtM Alloy Nanoparticles. *J. Phys. Chem. C* **2013**, *117*, 7294−7302.
(37) Zhu, Y.; Bu, L.; Shao, Q.; Huang, X. Subnanometer PtRh Nanowire with Alleviated Poisoning Effect and Enhanced C-C Bond Cleavage for Ethanol Oxidation Electrocatalysis. *ACS Catal.* **2019**, *9*, 6607−6612.
(38) Noguchi, T.; Sugiura, M. Analysis of Flash-Induced FTIR Difference Spectra of the S-State Cycle in the Photosynthetic Water-Oxidizing Complex by Uniform ^{15}N and ^{13}C Isotope Labeling. *Biochemistry* **2003**, *42*, 6035−6042.
(39) Zhang, T.; Zhang, Q.; Ge, J.; Goebl, J.; Sun, M.; Yan, Y.; Liu, Y.; Chang, C.; Guo, J.; Yin, Y. A Self-Templated Route to Hollow Silica Microspheres. *J. Phys. Chem. C* **2009**, *113*, 3168−3175.
(40) Wang, S.; Chen, M.; Wu, L. One-Step Synthesis of Cagelike Hollow Silica Spheres with Large Through-Holes for Macromolecule Delivery. *ACS Appl. Mater. Interfaces* **2016**, *8*, 33316−33325.
(41) Bouchoucha, M.; Gaudreault, R.-C.; Fortin, M.; Kleitz, F. Mesoporous Silica Nanoparticles: Selective Surface Functionalization for Optimal Relaxometric and Drug Loading Performances. *Adv. Funct. Mater.* **2014**, *24*, 5911−5923.
(42) Wan, Y.; Yu, S. Polyelectrolyte Controlled Large-Scale Synthesis of Hollow Silica Spheres with Tunable Sizes and Wall Thicknesses. *J. Phys. Chem. C* **2008**, *112*, 3641−3647.
(43) Makarovsky, I.; Boguslavsky, Y.; Alesker, M.; Lellouche, J.; Banin, E.; Lellouche, J. Novel Triclosan-Bound Hybrid-Silica Nanoparticles and their Enhanced Antimicrobial Properties. *Adv. Funct. Mater.* **2011**, *21*, 4295−4304.

https://dx.doi.org/10.1021/acsomega.0c06268
ACS Omega 2021, 6, 5846−5855

(44) Aliaga, C.; Park, J. Y.; Yamada, Y.; Lee, H. S.; Tsung, C.; Yang, P.; Somorjai, G. A. Sum Frequency Generation and Catalytic Reaction Studies of the Removal of Organic Capping Agents from Pt Nanoparticles by UV-Ozone Treatment. *J. Phys. Chem. C* **2009**, *113*, 6150−6155.
(45) Tan, B.; Lehmler, H. J.; Vyas, S. M.; Knutson, B. L.; Rankin, S. E. Fluorinated-Surfactant-Templated Synthesis of Hollow Silica Particles with a Single Layer of Mesopores in Their Shells. *Adv. Mater.* **2005**, *17*, 2368−2371.
(46) Wu, S.; Hung, Y.; Mou, C. Compartmentalized Hollow Silica Nanospheres Templated from Nanoemulsions. *Chem. Mater.* **2013**, *25*, 352−364.
(47) Han, Y.; Guo, Z.; Teng, S.; Xia, H.; Wang, D.; Han, M.; Yang, W. Rationalized Fabrication of Structure-Tailored Multishelled Hollow Silica Spheres. *Chem. Mater.* **2019**, *31*, 7470−7477.
(48) Yoshida, H.; Onodera, Y.; Fujita, S. I.; Kawamori, H.; Arai, M. Solvent effects in heterogeneous selective hydrogenation of acetophenone: differences between Rh/C and Rh/Al_2O_3 catalysts and the superiority of water as a functional solvent. *Green Chem.* **2015**, *17*, 1877−1883.
(49) Bertero, N. M.; Trasarti, A. F.; Apesteguía, C. R.; Marchi, A. J. Solvent effect in the liquid-phase hydrogenation of acetophenone over Ni/SiO_2: A comprehensive study of the phenomenon. *Appl. Catal., A* **2011**, *394*, 228−238.
(50) Trasarti, A. F.; Bertero, N. M.; Apesteguía, C. R.; Marchi, A. J. Liquid-phase hydrogenation of acetophenone over silica-supported Ni, Co and Cu catalysts: Influence of metal and solvent. *Appl. Catal., A* **2014**, *475*, 282−291.
(51) Shi, W.; Thompson, R. L.; Macala, M. K.; Resnik, K.; Steckel, J. A.; Siefert, N. S.; Hopkinson, D. P. Molecular Simulations of CO_2 and H_2 Solubility, CO_2 Diffusivity, and Solvent Viscosity at 298 K for 27 Commercially Available Physical Solvents. *J. Chem. Eng. Data* **2019**, *64*, 3682−3692.
(52) Shaw, J. M. A correlation for hydrogen solubility in alicyclic and aromatic solvents. *Can. J. Chem. Eng.* **1987**, *65*, 293−298.
(53) Valderrama, J. O.; Cortés, F. H.; Ibrahim, A. A.; Celiker, H. Literature Survey on Solubility Data of Hydrogen in Liquid Solvents. *Chem. Ing. Tech.* **1992**, *64*, 750−751.
(54) Trinh, T. K. H.; De Hemptinne, J. C.; Lugo, R.; Ferrando, N.; Passarello, J. P. Hydrogen Solubility in Hydrocarbon and Oxygenated Organic Compounds. *J. Chem. Eng. Data* **2016**, *61*, 19−34.
(55) Gao, X.; Tian, S.; Jin, Y.; Wan, X.; Zhou, C.; Chen, R.; Dai, Y.; Yang, Y. Bimetallic PtFe-Catalyzed Selective Hydrogenation of Furfural to Furfuryl Alcohol: Solvent Effect of Isopropanol and Hydrogen Activation. *ACS Sustainable Chem. Eng.* **2020**, *8*, 12722−12730.
(56) Dong, C.; Yu, Q.; Ye, R. P.; Su, P.; Liu, J.; Wang, G. H. Hollow Carbon Sphere Nanoreactors Loaded with PdCu Nanoparticles: Void-Confinement Effects in Liquid-Phase Hydrogenations. *Angew. Chem., Int. Ed.* **2020**, *59*, 18374−18379.
(57) Yang, T.; Wei, L.; Jing, L.; Liang, J.; Zhang, X.; Tang, M.; Monteiro, M. J.; Chen, Y. I.; Wang, Y.; Gu, S.; et al. Dumbbell-shaped bi-component mesoporous Janus solid nanoparticles for biphasic interface catalysis. *Angew. Chem., Int. Ed.* **2017**, *56*, 8459−8463.
(58) Jiang, P.; Chen, S.; Wang, C.; Wang, D.; Diao, J.; Cao, Z.; Lin, Z.; Luo, Q.; Lu, J.; Huang, H.; et al. Atomically dispersed Fe-N-S-C anchored on pomegranate-shaped carbon spheres for oxygen reduction reaction and all-solid-state zinc-air battery. *Mater. Today Sustainability* **2020**, *9*, No. 100039.
(59) Fung, C.; Tang, J.; Tan, L.; Mohamed, A. R.; Chai, S. Recent progress in two-dimensional nanomaterials for photocatalytic carbon dioxide transformation into solar fuels. *Mater. Today Sustainability* **2020**, *9*, No. 100037.
(60) Biesalski, M.; Johannsmann, D.; Rühe, J. Electrolyte-induced collapse of a polyelectrolyte brush. *J. Chem. Phys.* **2004**, *120*, 8807−8814.
(61) Wang, J.; Wang, J.; Ding, P.; Zhou, W.; Li, Y.; Drechsler, M.; Guo, X.; Cohen Stuart, M. A. A Supramolecular Crosslinker to Give Salt-Resistant Polyion Complex Micelles and Improved MRI Contrast Agents. *Angew. Chem., Int. Ed.* **2018**, *57*, 12680−12684.
(62) Yan, P.; Tian, P.; Li, K.; Cohen Stuart, M. A.; Wang, J.; Yu, X.; Zhou, S. Rh nanoclusters encaged in hollow mesoporous silica nanoreactors with enhanced catalytic performance for phenol selective hydrogenation. *Chem. Eng. J.* **2020**, *397*, No. 125484.
(63) Li, K.; Yang, C.; Yu, H.; Xiao, T.; Guan, W.; Ding, P.; Yin, H.; Cohen Stuart, M. A.; Wang, J.; Zhou, S. Coordination-Enhanced Synthesis for Hollow Mesoporous Silica Nanoreactors. *Chem. Mater.* **2020**, *32*, 2086−2096.

https://dx.doi.org/10.1021/acsomega.0c06268
ACS Omega 2021, 6, 5846−5855